water

MDPI

Article

Optimization of Pumping Station Inlet Channel Based on Stress-Blended Eddy Simulation Turbulence Model and Entropy Generation Theory

Rui Jiang [1], Yi Zhang [2], Jianzhong Zhu [3], Buqing Chen [4], Yiping Tang [5], Xu Yang [6], Yuan Zheng [1,6,*] and Huiling Duan [1,*]

1 School of Electrical and Power Engineering, Hohai University, Nanjing 211100, China; 231306020006@hhu.edu.cn
2 Haining Yancang River Dike Management Office, Haining 314400, China; youyou2003nb@163.com
3 Management Service Center of Hangjiahu South Drainage Project, Jiaxing 314000, China; 13666765730@163.com
4 Jiaxing Hydrological Station, Jiaxing 314000, China; 15257383075@163.com
5 Haining Water Resources Bureau, Haining 314400, China; typ1846@126.com
6 College of Water Conservancy and Hydropower Engineering, Hohai University, Nanjing 210098, China; 231302030021@hhu.edu.cn
* Correspondence: zhengyuan@hhu.edu.cn (Y.Z.); duanhuiling@hhu.edu.cn (H.D.)

Abstract: The optimization of pumping station inlet channels is a key research area for improving the operation efficiency, reducing the energy consumption, and enhancing the operation reliability of pumping stations. For the elbow inlet channel of the Majinggang Pumping Station project, based on the Stress-Blended Eddy Simulation (SBES) turbulence model and entropy generation theory, an optimization design plan is proposed by altering the inclination angle of the flow channel base plate, the length of the transitional arc segment, and the length of the curved segment. Various schemes were analyzed and comprehensively compared in terms of the hydraulic loss, the velocity-weighted average angle, and the axial-velocity distribution uniformity of the channel. The results indicate that optimal hydraulic performance is achieved when the inclination angle of the base plate is between 8° and 10°. In a reasonable range of values, appropriately increasing the length of the transitional arc and reducing the section width (throat width) can improve the hydraulic performance of the inlet channel. The optimal model obtained achieved an impressive velocity-weighted average angle of 89.25°, along with an axial-velocity distribution uniformity of 97.5%. Its excellent hydraulic performance not only meets the design requirements of the pumping station in terms of functionality but also takes into account economic efficiency, and it serves as a valuable reference for similar projects, contributing to the more refined and intelligent development of the optimization of pumping station inlet flow channels.

Keywords: SBES; entropy generation theory; inlet channel; numerical simulation; hydraulic performance

check for updates

Academic Editor: Silvia Di Francesco

Received: 18 December 2024
Revised: 17 January 2025
Accepted: 27 January 2025
Published: 30 January 2025

Citation: Jiang, R.; Zhang, Y.; Zhu, J.; Chen, B.; Tang, Y.; Yang, X.; Zheng, Y.; Duan, H. Optimization of Pumping Station Inlet Channel Based on Stress-Blended Eddy Simulation Turbulence Model and Entropy Generation Theory. *Water* **2025**, *17*, 378. https://doi.org/10.3390/w17030378

Copyright: © 2025 by the authors. Licensee MDPI, Basel, Switzerland. This article is an open access article distributed under the terms and conditions of the Creative Commons Attribution (CC BY) license (https://creativecommons.org/licenses/by/4.0/).

1. Introduction

An inlet channel, a crucial component of a water pump system, is designed to gradually accelerate the water flow from the forebay and ensures a smooth entry into the impeller chamber after changing the flow direction [1,2]. The flow state within the inlet channel directly determines the suction conditions of the pump, and the utilization efficiency of the

incoming flow energy has a direct effect on the overall hydraulic efficiency of the pump installation [3]. Therefore, research on the flow state within inlet channels is particularly important [4–7]. With the acceleration of global urbanization and the continuous advancement of infrastructure construction, the market demand for high-flow pumping stations continues to grow. These stations are increasingly being applied across diverse sectors such as agricultural irrigation, urban water supply systems, firefighting, and emergency rescue [8]. To enhance the drainage capacity from the eastern plains to the Qiantang River, a new high-flow pumping station (Majinggang Pumping Station) with a design flow rate of 150 m^3/s has been constructed in Haining, Jiaxing, China.

For a long time in the past, the optimization of pumps and other fluid machinery was conducted mainly through experimental methods [9–12]. Experimental errors are difficult to avoid, and in order to address this issue, Jiang et al. [13] introduced a new error analysis method, which judges the accuracy of data by observing whether fluctuations in data during an experiment is within the expected theoretical error range. At the same time, experimental methods often entail significant costs and require stringent environmental conditions. In recent years, the swift advancement of Computational Fluid Dynamics (CFD) technology has tackled this challenge [14,15], leading to notable progress in both theoretical exploration and engineering applications for the optimal design of inlet and outlet channels in pumping stations. The application of flow field analysis methods in the optimization of pumping station channels has become increasingly widespread [16,17]. Through CFD simulation technology, researchers can precisely forecast the flow characteristics within the channel of pumping stations, identify detrimental factors in the flow field like vortices, backflow, and pressure losses, and consequently provide a scientific basis for channel optimization. In Ref. [18], researchers optimized the flow channel of a conical axial maglev blood pump. The improved channel design facilitates smoother fluid flow inside the pump, reducing the impact and wear on the pump's impeller. Shrestha and Choi [19] conducted a thorough analysis of the reverse flow phenomenon within the J-groove channels of AJP and SCP models, discovering that reverse flow is influenced by various factors, including the geometric shape of the channel, fluid parameters, and boundary conditions. Utilizing the CFD method, Sujono et al. [20] reduced the cavitation at the Ciawi Dam inlet conduit. Cheng [21] proved the guide splitter significantly adjusts the distribution of momentum in the diversion channel. Xie et al. [22] employed numerical simulations to explore methods for controlling the flow separation phenomenon in the inlet channels of pumping stations. Additionally, through experiments, he verified the effect of optimizing geometric parameters such as the inclination angle of a flow channel bottom plate and the length of the transition arc section on suppressing flow separation.

In numerical simulations, hydraulic loss, the velocity-weighted average angle, and axial-velocity distribution uniformity are important indices for evaluating the hydraulic performance of pumps. Ref. [23] evaluated the hydraulic performance of nuclear main pumps using the inlet-section velocity-weighted average angle as a criterion. Ref. [24] determined the optimal size of the stationary diffuser for an axial-flow pump, with the axial-velocity distribution uniformity at the outlet section as the response objective. Yu et al. [25], based on the velocity-weighted average angle and axial-velocity distribution uniformity, introduced a comprehensive assessment indicator for the flow pattern in the forebay of pumping stations. The theory of entropy production is capable of evaluating the extent of hydraulic losses, pinpointing the primary locations of these losses, and holds significant importance for enhancing hydraulic efficiency. Li et al. [26] investigated the efficiency of liquid ring vacuum pumps by examining hydraulic losses, uncovering the underlying mechanism of these losses, and exploring their magnitude and distribution through the application of entropy generation theory. Ji et al. [27] adopted the entropy generation

method to visualize the energy losses in a mixed-flow pump with guide vanes, thus proving that tip clearance is closely related to the external characteristic performance of a mixed-flow pump. Zhou et al. [28] wrote a review on the application of the entropy production theory in hydraulic machinery, where he not only delved into the role of the entropy production theory and its research status but also made a prospect for the future. Scholars have also employed advanced optimization algorithms such as genetic algorithms and particle swarm optimization, combined with CFD simulation results, for a multi-objective optimization design [29–31]. The selection of turbulence models greatly affects the accuracy, stability, and efficiency of calculations [32,33], with widely used models including k-ε, k-omega, RNG, and SST. Using the RNG turbulence model, Tian [34] compared the hydraulic losses and internal flow patterns in the water tank of five cases to determine the best solution. Hao and Tan [35] compared the cavitation characteristics of pumps with symmetric and asymmetric tip clearances using the SST k-ω model, concluding that the clearance at the pump blade tips exerts a notable influence on the cavitation characteristics of mixed-flow pumps, and performance is more adversely affected by asymmetric tip clearances.

Traditional turbulence models have certain limitations, especially in simulating wall flow characteristics. The emergence of improved new turbulence models is gradually overcoming these deficiencies. Gul et al. [36] presented a Two-Time-Scale turbulence model. Sun et al. [37] enhanced the G-Y turbulence model, which can reasonably predict the development process of boundary layers and transition locations. Kan et al. [38] investigated the turbulence statistics of an axial-flow pump across varying flow velocity conditions based on large-eddy simulations. In Ref. [39], the double-hump characteristic was accurately predicted when using the SAS model. Among the improved models, the Stress-Blended Eddy Simulation (SBES) model merges the strengths of the Reynolds-Averaged Navier–Stokes (RANS) model and the large-eddy simulation (LES) method, which is increasingly adopted. Ref. [40] demonstrated that the SBES method is best suited for scenarios involving a combination of boundary layers and free shear flows. Zore et al. [41] pointed out that High-Fidelity SBES simulations provide precise forecasts of both the development of a jet plume and the gradual buildup of turbulent kinetic energy within it. The research of ref. [42] showed that the SBES model is especially skilled at depicting three-dimensional vortex structures that form behind pins. According to engineering reality and the advantages and disadvantages of each model, SBES was finally selected for smooth simulations in this paper.

Although previous research has optimized the inlet channels of pumping stations using experimental methods and CFD technology, most of these studies have been centered around the adjustment of a single geometric parameter or specific types of pumping stations. However, this study is centered around the elbow-shaped inlet channel of the Majingang Pumping Station. This inlet channel has a specific design flow rate and a complex geometric structure. By comprehensively applying the SBES turbulence model and entropy generation theory and taking into account multiple factors such as variations in the inclination angle of the flow channel bottom plate, the length of the transition arc section, and the length of the curved section, this study conducts a systematic analysis of the impact of different design schemes on hydraulic performance. This multi-parameter and multi-dimensional optimization approach represents a pioneering attempt in the optimization of similar pumping station inlet channels. It offers new ideas and references for the refined and intelligent design of such channels. From a theoretical perspective, this research not only validates the applicability and accuracy of the SBES turbulence model in simulating the flow field of complex pumping station inlet channels but also expands the applicational scope of the entropy generation theory in the optimization of pumping station inlet channels. It provides a theoretical basis and methodological reference for subsequent related research.

From a practical perspective, the optimized design schemes and performance prediction results obtained in this study can be directly applied to the construction of the Majingang Pumping Station. This application can enhance its operational efficiency and reliability, can reduce energy consumption, and thus has significant value in engineering applications. Meanwhile, these achievements also serve as reference cases for the optimized design of other similar pumping station inlet channels, contributing to the technological advancement and sustainable development of the pumping station industry.

2. Geometric Model and Numerical Simulations

2.1. Research Object

The design flow rate of the Majinggang Pumping Station is 150 m^3/s, and under extreme conditions, it is 180 m^3/s. The pumping station selects 6 vertical mixed-flow pumps with a positive water inlet, the design flow rate of a single pump is 30.0 m^3/s, the head is 9.55 m, and the rotational speed is 115.4 r/min. In this paper, the inlet flow of individual pumps is used as the research object.

2.2. Geometric Model

Based on the provided project data, the width of the elbow inlet channel is 7.5 m, and the length from the pump centerline to the end of the channel is 30 m. Utilizing existing CAD drawings and pump design parameters, the inlet channel was modeled using the UG NX 2000 modeling software. The geometric model of the inlet channels for different design schemes are similar. Taking the initial scheme as an example, the geometric model is shown in Figure 1.

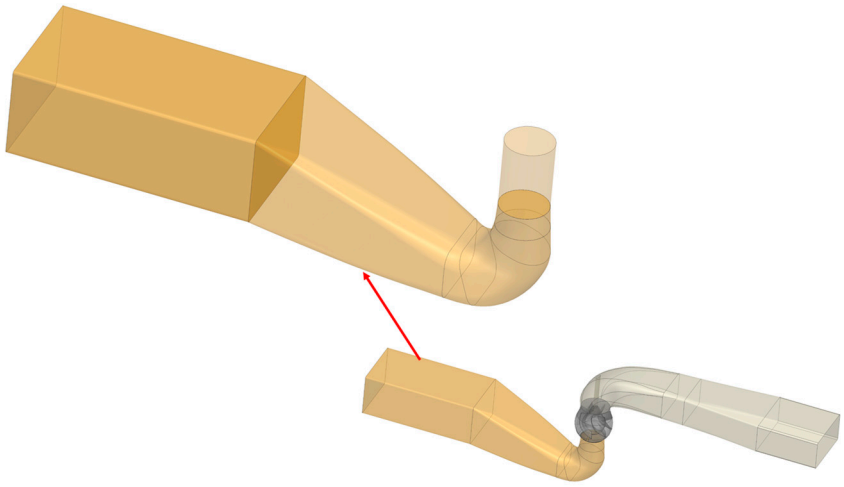


Figure 1. Geometric model of inlet channel.

2.3. Meshing

Using the ICEM 2023 software for mesh generation, a higher-precision and better-quality hexahedral-structured mesh was utilized for the computational section [43], with the mesh schematic shown in Figure 2. At the same time, to avoid wasting computational time and resources by using excessively fine meshes and to improve the trustworthiness of the outcomes, a mesh independence validation was conducted on the model using head loss as the standard for evaluation. The results are shown in Table 1 and Figure 3. When the number of meshes in the computational domain reaches 1.36×10^6 (i.e., the red dot in the figure), the curve tends to flatten. When it exceeds 1.5×10^6, the hydraulic loss reaches a stable state. Therefore, the number of meshes used in this computation was set to 1.5×10^6.

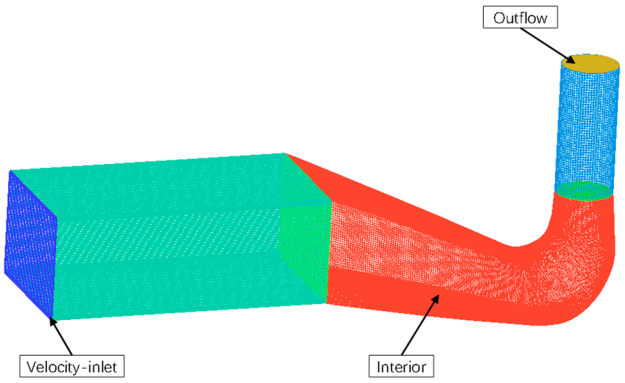


Figure 2. Computational domain meshing.

Table 1. Mesh independence verification.

Mesh Size (mm)	Mesh Type	Mesh Count (10^6)	Hydraulic Loss (m)	Percentage
600	Hexahedron	0.250	0.24511	
300	Hexahedron	0.499	0.22830	7.36%
210	Hexahedron	0.713	0.21572	5.83%
165	Hexahedron	0.908	0.20889	3.27%
125	Hexahedron	1.199	0.20611	1.35%
110	Hexahedron	1.362	0.20562	0.25%
95	Hexahedron	1.577	0.20555	0.02%
85	Hexahedron	1.763	0.20550	0.02%
60	Hexahedron	2.497	0.20550	0

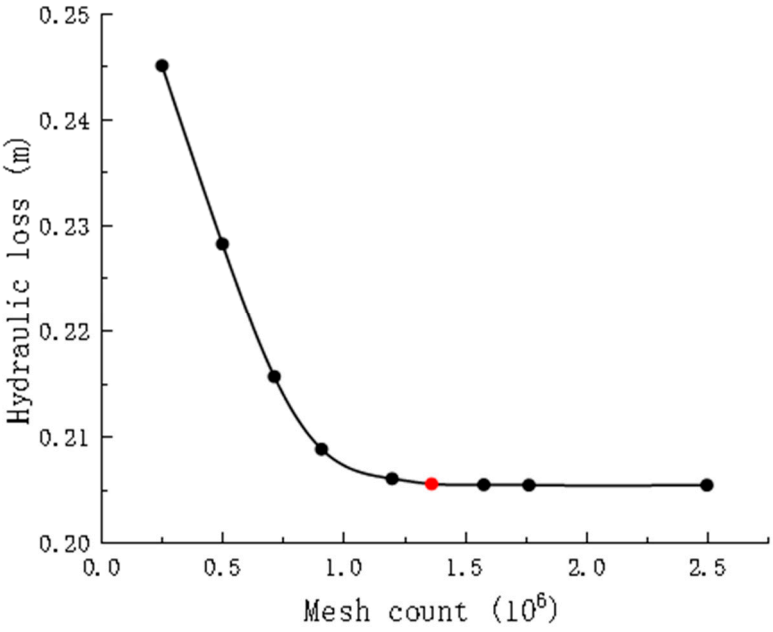


Figure 3. Mesh independence verification.

2.4. Turbulence Model

In numerical simulations, the most widely used turbulence models include k-ε, k-ω, SST, etc. The k-ε model is characterized by high computational efficiency and wide applications. However, when it comes to simulating complex boundary-layer flows and separated flows, its accuracy is relatively low. As a result, it has difficulty in accurately capturing the flow separation and vortex phenomena that may occur in the inlet channel

of a pumping station. The k-ω model has made improvements in simulation accuracy in the near-wall region. Nevertheless, when handling large-scale turbulent structures and free-shear-layer flows, it still exhibits certain limitations. Thus, it may not be able to fully reflect the complex turbulent characteristics within the inlet channel of a pumping station. In some scenarios, the RNG k-ε model can enhance the simulation of turbulence. However, its handling of boundary-layer flows remains insufficiently refined. Additionally, when simulating flows in complex geometric configurations, its computational stability may be compromised. The SST k-ω model integrates the advantages of the k-ω and k-ε models, demonstrating good simulation capabilities for both wall-adjacent flows and free-shear-layer flows [44–46]. However, when faced with complex flows featuring strong flow separation and re-attachment phenomena, its prediction accuracy and stability still require further enhancement.

As a hybrid RANS–LES turbulence model, the SBES model combines the high efficiency of the RANS model with the high accuracy of the LES model. In the near-wall region, the SBES model uses the RANS model for an efficient simulation, enabling it to accurately capture the detailed characteristics of boundary-layer flows. In the region far from the wall, the SBES model switches to the LES mode, directly simulating turbulent vortex structures with high precision. This allows for a comprehensive and accurate simulation of complex turbulent flows in the inlet channel of a pumping station, including boundary-layer flows and free-shear-layer flows, and possible flow separation and eddy phenomena. Moreover, the SBES model has good adaptability and flexibility. It can automatically adjust the calculation accuracy of the model according to flow characteristics, further improving the reliability and accuracy of the simulation.

$$\boldsymbol{\tau}_{ij,SBES} = \boldsymbol{\tau}_{ij,RANS} f_{SBES} + \boldsymbol{\tau}_{ij,LES}(1 - f_{SBES}) \quad (1)$$

$$\boldsymbol{\mu}_{t,SBES} = \boldsymbol{\mu}_{t,RANS} f_{SBES} + \boldsymbol{\mu}_{t,LES}(1 - f_{SBES}) \quad (2)$$

In the above equation, f_{SBES} is the shielding function; $\boldsymbol{\tau}_{ij,SBES}$, $\boldsymbol{\tau}_{ij,RANS}$, and $\boldsymbol{\tau}_{ij,LES}$, respectively, represent the stress tensors for SBES, RANS, and LES; while $\boldsymbol{\mu}_{t,SBES}$, $\boldsymbol{\mu}_{t,RANS}$, and $\boldsymbol{\mu}_{t,LES}$, respectively, denote the turbulent dynamic viscosities for SBES, RANS, and LES.

The primary benefit of the SBES model is that it allows the LES portion of the flow to use a specific LES model, rather than relying on the LES capabilities of models like DES. Additionally, it makes the RANS solution in the boundary layer independent of grid resolution, and it can be used to visually display the application regions of the LES and RANS models, facilitating the verification of consistent settings.

2.5. Boundary Conditions and Calculation Methods

In this study, the inlet boundary condition is set as a mass flow rate inlet. This setting can accurately reflect the flow rate input during the actual operation of a pumping station, ensuring that the simulated flow rate is consistent with the designed flow rate in a practical scenario. As for the outlet boundary condition, it is set as a pressure outlet. This setting can effectively simulate the pressure environment at the outlet of the pumping station, ensuring that the simulated pressure matches the actual pressure in real-world situations. The SBES model is employed as the turbulence model, which can fully capture the flow characteristics of the wall boundary layer and can simulate real flow patterns, thus eliminating the need for special treatment of the wall surface. The SIMPLEC method is employed to solve the velocity–pressure coupling.

2.6. Hydraulic Performance Evaluation Index

Hydraulic loss, the velocity-weighted average angle, and axial-velocity distribution uniformity were adopted as the evaluation indices for the hydraulic performance of the flow channel, and a weighted evaluation function is proposed.

2.6.1. Hydraulic Loss

Hydraulic loss reflects the energy dissipation of water flowing through an inlet passage. A smaller hydraulic loss indicates less energy dissipation and a more economical operation of the pumping station. Drawing from Bernoulli's energy equation, the notion of hydraulic loss (Δh) is introduced. The hydraulic loss of flow components is predicted using the velocity and pressure fields derived from CFD numerical simulations.

$$\Delta h = E_1 - E_2 = \left(\frac{P_1}{\rho g} - \frac{P_2}{\rho g} + Z_1 - Z_2\right) + \left(\frac{u_1^2}{2g} - \frac{u_2^2}{2g}\right) \tag{3}$$

$$E_1 = \frac{P_1}{\rho g} + Z_1 + \frac{u_1^2}{2g};\ E_2 = \frac{P_2}{\rho g} + Z_2 + \frac{u_2^2}{2g} \tag{4}$$

In this formula, E_1 represents the total energy at the inlet of the flow channel, while E_2 denotes the total energy at the outlet of the flow channel.

2.6.2. Entropy Production Theory

In thermodynamics, irreversible processes lead to an increase in entropy, and this increment in entropy resulting from irreversibility is referred to as entropy production. In recent years, the entropy production theory has been extensively applied in the analysis of internal flow losses and stability in hydraulic machinery [47]. It is characterized by ease of capture, visualization, and precise localization, making it a highly effective method for revealing the mechanisms of energy loss within fluid machinery. For turbulent flows, entropy production rates can be segmented into two components: one is the direct dissipation term caused by the average velocity, known as direct entropy production; the other is the turbulent dissipation term caused by fluctuating velocities, known as indirect entropy production, defined as follows:

$$\dot{S}_D''' = \dot{S}_{\overline{D}}''' + \dot{S}_{D'}''' \tag{5}$$

In this equation, $\dot{S}_D'''$ represents the total entropy production rate, $\dot{S}_{\overline{D}}'''$ is the entropy production rate caused by the mean velocity, and $\dot{S}_{D'}'''$ denotes the entropy production rate resulting from velocity fluctuations.

2.6.3. Axial-Velocity Distribution Uniformity

Axial-velocity distribution uniformity indicates the degree of uniformity in the velocity distribution of a fluid during its flow. A closer approximation of 100% in the uniformity of the axial-velocity distribution at the inlet channel of a pump segment reflects better uniformity and stability of the water flow. A new formula for the uniformity of axial-velocity distribution based on area averaging is introduced, which takes into account the influence of infinitesimal area elements. Since the infinitesimal area elements near the boundary layer with lower velocities are smaller, their product values are much smaller than those in the turbulent region, which, to some extent, diminishes the mesh reliance of the calculation results. The new formula is as follows:

$$\boldsymbol{v}_u = \left(1 - \frac{1}{\overline{\boldsymbol{u}_a}\overline{\boldsymbol{A}_a}}\sqrt{\sum\left(\boldsymbol{u}_{ai}\boldsymbol{A}_{ai} - \overline{\boldsymbol{u}_a}\boldsymbol{A}_{ai}\right)/n}\right) \times 100\% \tag{6}$$

$$\overline{\boldsymbol{u}_a} = \frac{\sum(\boldsymbol{V}_{ai}\boldsymbol{A}_{ai})}{\sum \boldsymbol{A}_{ai}};\ \overline{\boldsymbol{A}_a} = \frac{\sum \boldsymbol{A}_{ai}}{n} \tag{7}$$

In the above equation, $\boldsymbol{V}_u$ represents the axial-flow velocity distribution uniformity in the outlet section, while the axial-velocity of the computational unit in the outlet section is denoted by $\boldsymbol{V}_{ai}$. $\boldsymbol{A}_{ai}$ indicates the area of the microelement, while $\boldsymbol{u}_{ai}$ indicates the axial-velocity of the microelement control body. n is the number of computational units in the outlet section.

2.6.4. Velocity-Weighted Average Angle

The velocity-weighted average angle reflects the average direction of the water flow velocity vector. A closer approximation of 90° in the uniformity of axial-velocity distributions indicates smaller cross-flow values and better hydraulic performance. The calculation formula is as follows:

$$\theta = \sum_{i=1}^{n} \boldsymbol{V}_{ai}(90^\circ - tg^{-1}\frac{\boldsymbol{V}_{ti}}{\boldsymbol{V}_{ai}}) / \sum_{i=1}^{n} \boldsymbol{V}_{ai} \tag{8}$$

In this formula, θ is the velocity-weighted average angle of outlet flow, while $\boldsymbol{V}_{ti}$ represents the tangential velocity of the computational unit of the outlet section.

2.6.5. Weighted Evaluation Function

In the inlet channel of a pumping station, hydraulic loss is a key indicator because it directly affects the operating efficiency and energy consumption of the pumping station. A larger hydraulic loss means that more energy is required to push water into the pump, thereby increasing the operating cost of the pumping station. Moreover, a higher hydraulic loss may lead to an excessive pressure drop in the inlet flow passage, which affects the suction performance of the pump and may cause adverse phenomena such as cavitation. Therefore, we determined the weight of hydraulic loss to be 0.5.

Velocity distribution uniformity and the velocity-weighted average angle are also of great significance for a pumping station. Unreasonable water flow angles or uneven velocity distributions may cause greater impacts on the impeller, pump casing, and other components of a pump, thus affecting the service life and reliability of the equipment. However, in a comprehensive evaluation, their importance may be slightly lower compared with hydraulic loss, and their weights were finally assigned the value of 0.25, respectively.

After determining the weights of each part, a weighted evaluation function is proposed:

$$E = 0.5k_1h + 0.25k_2\frac{\theta}{90^\circ} + 0.25k_3v_u \tag{9}$$

$$K_1 = \frac{1}{h_{min} - h_{max}},\ K_2 = \frac{1}{\frac{\theta}{90^\circ}_{max} - \frac{\theta}{90^\circ}_{min}},\ K_3 = \frac{1}{v_{umax} - v_{umin}} \tag{10}$$

In this formula, the purpose of introducing k is to make the changing values of various physical quantities within the same range.

3. Preliminary Design of Inlet Channel

An elbow-shaped inlet channel is shown in Figure 4, which is generally composed of a straight section, a curved section, and a conical outlet section. The control dimensions of an elbow-shaped inlet channel profile include the following: width (B_j), length (X_L), height (H_w), throat height of the passage (H_k), length of the straight section (X_{z1}), length of the curved section (X_w), length of the transition arc segment (X_r), inlet height of the passage (H_j), inclination angle of the upper plate (α), inclination angle of the base plate (β), etc.

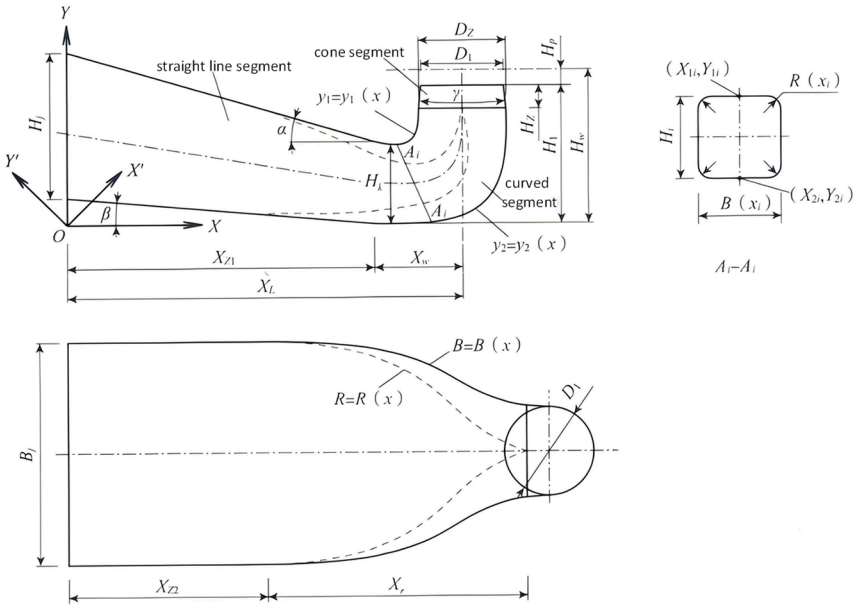


Figure 4. Geometric parameters of elbow inlet channel.

Both Ref. [22], mentioned above, and an article recently published by Zhang et al. [48] conducted research on elbow-shaped inlet channels. From these studies, it can be concluded that the initial design parameters, including H_k, were reasonably chosen. This optimization primarily focuses on β and X_r, with minor adjustments made to X_w (in Scheme 0, 3377.0 mm represents the distance from the upper inlet of the elbow section in the side view of Figure 4 to the centerline, and 2282.7 mm denotes the distance from the lower inlet of the elbow section to the centerline). The inlet channel's gradually reducing section employs an arcuate taper design, and a total of 9 optimized inlet channel schemes were devised, with a conventional design flow rate (Q) of 30. The specific parameters for each scheme are presented in Table 2.

Table 2. Specific parameters for the inlet channel.

	X_w (mm)	X_r (mm)	β (°)	Q (m^3/s)
0	3377.0/2282.7	10,604.2	8	30
1	3377.0	10,604.2	10	30
2	3377.0/2282.7	10,604.2	10	30
3	3554.8/1809.7	10,604.2	8	30
4	3554.8/1809.7	11,550.3	8	30
5	3554.8/1809.7	11,550.3	10	30
6	3554.8	9798.4	8	30
7	3554.8/1890.7	9798.4	8	30
8	3554.8/1809.7	9798.4	4	30
9	3554.8	9798.4	8	30

The hydraulic losses of the initial model and the optimized models under rated conditions were compared. From this comparison, four schemes, namely, 2, 3, 4, and 5, were selected for further evaluation and calculation. The specific data are shown in Table 3.

Table 3. Specific parameters of the preferred scheme for inlet channel.

	X_w (mm)	X_r (mm)	β (°)	Q (m^3/s)
JS0	3377.0/2282.7	10,604.2	8	30
JS1	3554.8/1809.7	11,550.3	10	30
JS2	3377.0/2282.7	10,604.2	10	30
JS3	3554.8/1809.7	10,604.2	8	30
JS4	3554.8/1809.7	11,550.3	8	30

3.1. Calculation of Inlet Channel Flow Characteristics

The CFD numerical modeling method was used to carry out a hydrodynamic analysis of the above five design schemes to verify the feasibility of the optimization scheme, and then, a more reasonable basis for improvement of the optimization scheme was proposed. The inlet and outlet sections were selected to calculate the hydraulic losses in the inlet flow channel across various flow conditions, as shown in Figure 5.

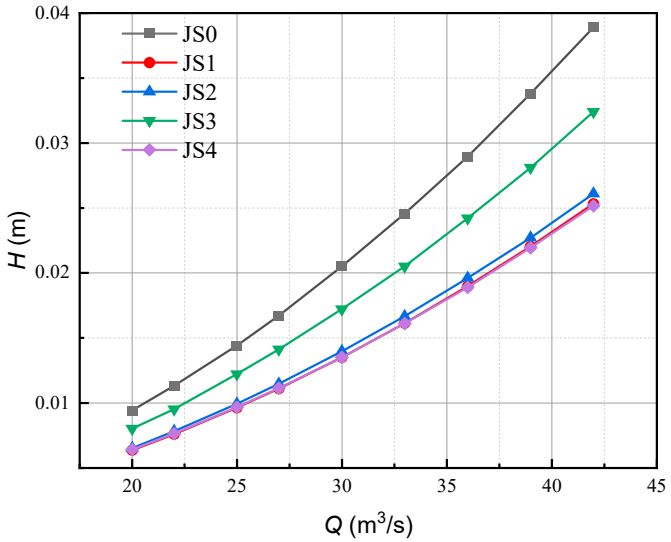


Figure 5. Hydraulic loss–flow rate curve.

As shown in Figure 5, there is a positive correlation between hydraulic loss and the flow rate across different schemes, with hydraulic loss increasing as the flow rate increases. In the inlet channel of a vertical mixed-flow pump, the primary component of hydraulic loss is along the flow path. The water inlet has an approximately square section that gradually transitions to a circular section at the elbow, where the flow velocity rapidly increases. Given the same loss coefficient, this results in greater head loss. The varying positions of the converging sections and the gradual alterations in the cross-sectional area of the elbow section across different schemes lead to differing hydraulic losses under the same flow conditions. In the transition zone at the middle of the elbow, moderate contraction of the flow helps reduce loss. However, excessive contraction can cause disordered flow mixing, affecting the inlet flow pattern. Within a reasonable range of X_r values, the hydraulic loss of each optimized scheme decreases as X_r increases. When the inclination angle of the base plate (β) is between 8° and 10°, optimal hydraulic loss is achieved. Based on the above analysis, JS1 and JS4 have the smallest hydraulic losses.

Thereafter, the velocity distribution at this cross-section was obtained, followed by the calculation of the velocity-weighted average angle and axial-velocity distribution uniformity, as presented in Figures 6 and 7.

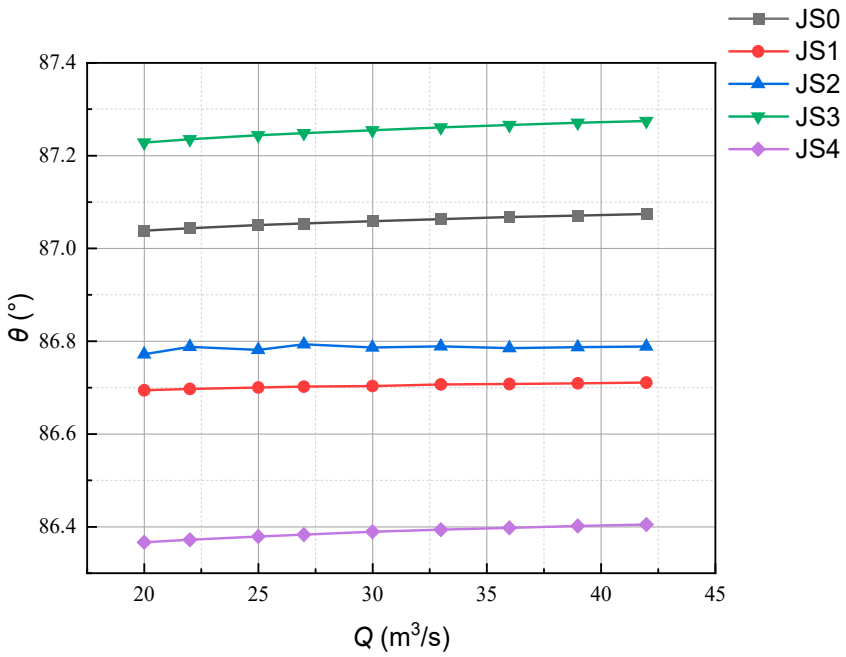


Figure 6. Velocity-weighted average angle–flow rate curve.

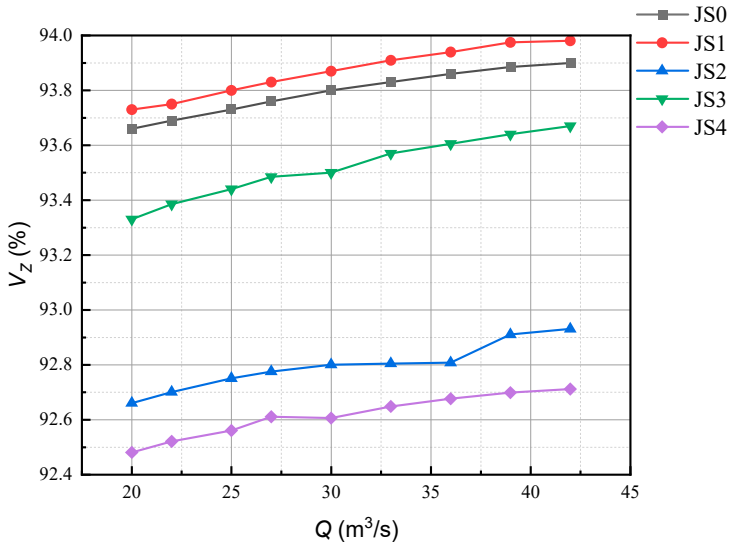


Figure 7. Axial-velocity distribution uniformity–flow rate curve.

Figure 6 illustrates that, excluding the influence of the impeller, the difference in the velocity-weighted average angle for the same scheme under various flow rates is relatively small and hardly varies with the flow conditions. When the water flow enters the elbow section, the flow velocity increases rapidly due to a compression effect, with the highest velocity occurring on the inner side of the elbow. After the turn, the velocity gradually shifts to the axial direction and the circumferential velocity decreases due to the channel, leading to a decrease in the axial-velocity-weighted average angle. The velocity-weighted average angle of Scheme JS3 is better than that of the initial scheme, and Scheme JS1's is notably superior to Scheme JS4's.

Figure 7 shows that the trend in section uniformity across different schemes is consistent with the trend in the velocity-weighted average angle. For the same scheme, there is little variation in the axial-velocity distribution uniformity curve across varying flow conditions. After going through the elbow section, the velocity of the water flow shifts to the axial direction. The velocity of the flow is greater on the inside of the elbow and

slower on the outside, and the velocity distribution gradually grows more uniform after the turn. Comparing different design schemes, the axial-velocity distribution uniformity of the optimized scheme JS1 is better than that of the original scheme.

After obtaining the values for hydraulic loss, the velocity-weighted average angle, and velocity distribution uniformity, weighted values were calculated under the rated flow rate according to Equations (9) and (10).

From Table 4, we can clearly conclude that the hydraulic performance of JS1 is significantly superior to that of other schemes.

Table 4. Hydraulic performance weighted value.

	H (m)	θ (°)	v_z (%)	E
JS0	0.0205	87.0584	93.80	42.1961
JS1	0.0135	86.7027	93.87	42.6073
JS2	0.0140	86.7859	92.80	42.3870
JS3	0.0172	87.2547	93.50	42.4288
JS4	0.0135	86.3883	92.61	42.2666

3.2. Flow Field Analysis Inside the Inlet Channel

The CFD calculations were performed on different optimized schemes under the design flow conditions to obtain the flow-field-distribution information within the inlet channel. The streamlines of the forebay section and the extended outlet section are smooth, and the velocity variation is uniform, so only the inlet channel section was analyzed. Figure 8 gives a streamline chart of different inlet channel schemes, Figure 9 shows the velocity cloud of the longitudinal section of the runner, while Figure 10 indicates the corresponding pressure cloud. (Figures 8–10 show only the initial scheme and the JS1 and JS3 schemes with relatively high weighted scores.)

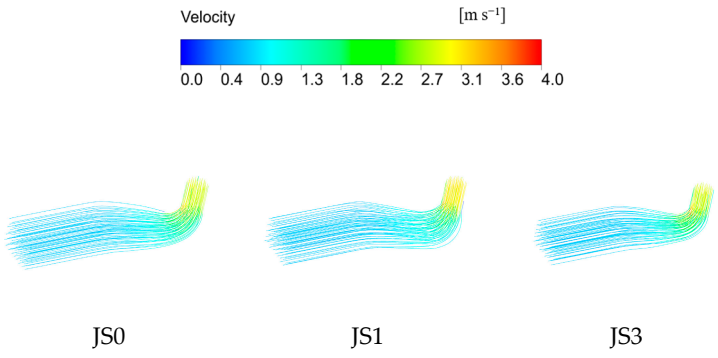


Figure 8. Streamline chart for inlet channel.

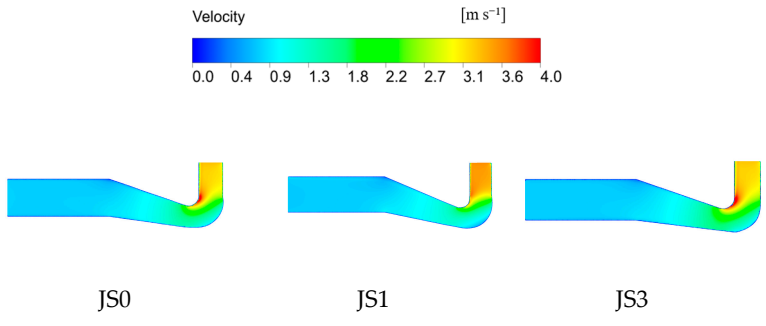


Figure 9. Inlet channel velocity cloud.

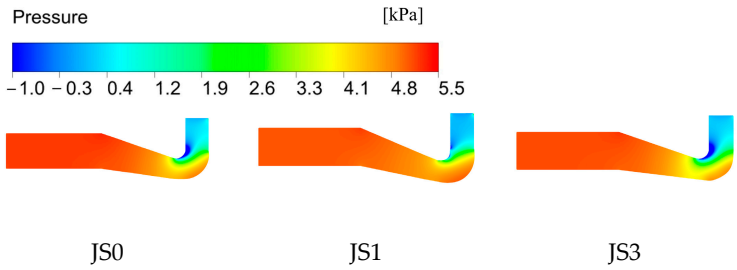


Figure 10. Inlet channel pressure cloud.

As illustrated in Figure 8, the streamline chart for the inlet channel is smooth, and the overall flow pattern is satisfactory. Under the condition of a normal design flow, as the cross-sectional area decreases, the flow velocity gradually increases. At the elbow, the flow velocity rapidly accelerates, with a higher velocity on the inner side and a lower velocity on the outer side. The streamlines are relatively smooth, with no vortex or backflow phenomena observed. The difference between the streamlines of different programs is relatively small.

Figure 9 indicates that the velocity clouds of the channel of each scheme are consistent with the distribution of the runner streamlines, and the velocity clouds can reflect the velocity distribution of the longitudinal cross-section more clearly. In the initial segment of the flow channel in the bent-elbow section, the velocity gradually increases as the cross-sectional area decreases; the direction of the flow velocity changes at the bent elbow; the flow velocity increases rapidly, showing a large inside and a small outside; and after the turn, the velocity turns to the axial direction and is gradually distributed uniformly, and the trend of the change of the cloud of each scheme is consistent. The velocity clouds under the design flow conditions reveal that in the JS1 scheme, there is no red area with a sudden velocity change on the inner side of the elbow. The velocity transition is more uniform, which is significantly superior to other schemes.

Figure 10 indicates that as the section gradually shrinks, the flow velocity increases, and the section pressure decreases, with a small pressure on the inside and a large pressure on the outside at the bent elbow. By comparing the pressure distribution at the longitudinal section with the velocity distribution, it was found to be correlated with the velocity, i.e., the velocity is smaller in the region with a large pressure distribution. The uniformity of pressure distribution of the optimized scheme is significantly better than that of the initial scheme, with the JS1 scheme being the most uniform.

To more intuitively reflect the pressure and velocity changes between the optimized JS1 scheme and the initial JS0 scheme, we selected five cross-sectional areas from the inlet to the outlet, labeled as V1 to V5, as shown in Figure 11. We calculated the velocity and pressure at the rated flow rate, and the results are presented in Table 5. As can be seen from this table, the velocity of the optimized scheme at each cross-section increased to some extent. This is mainly because the inclination angle of the flow channel bottom plate and the length of the transition arc section were optimized, enabling the fluid to flow more smoothly in the elbow-bend section. This reduces the occurrence of flow separation and eddy current phenomena, thus improving velocity uniformity. The decrease in pressure is due to the fact that the optimized scheme reduces the local resistance of the fluid in the elbow-bend section, minimizing the kinetic energy loss of the fluid. As a result, the fluid flows more efficiently in this area, thereby reducing the pressure loss. The increase in velocity and the decrease in pressure fully demonstrate that the optimized scheme can improve the operating efficiency of the pumping station and reduce energy consumption.

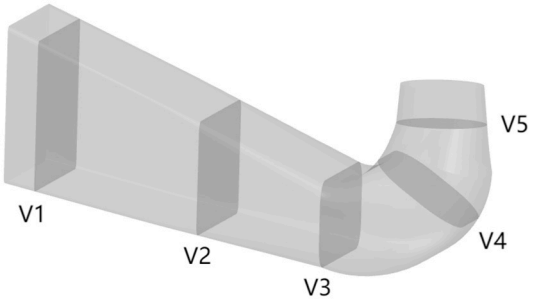


Figure 11. Cross-sectional view of the inlet channel.

Table 5. Cross-sectional average velocity and pressure.

	V-JS0 (m/s)	V-JS1 (m/s)	P-JS0 (kPa)	P-JS1 (kPa)
V1	0.84	0.87	5.27	5.03
V2	1.09	1.13	4.94	4.79
V3	1.33	1.39	4.33	4.12
V4	2.45	2.58	2.01	1.88
V5	3.17	3.49	0.52	0.35

The velocity distribution at the pump inlet channel directly affects the working efficiency and stability of the water pump. When the velocity distribution is uneven, local vortices or turbulent flows may occur, which increases the friction and resistance within the fluid. A uniform velocity distribution enables the pump to operate more smoothly, reduces the impact on the impeller and other components, and decreases the likelihood of cavitation. Figure 12 shows the velocity cloud at the inlet section of the water pump for the initial scheme (JS0) and the optimal scheme (JS1) among the optimized schemes. As can be seen from the figure, the velocity distribution of the optimized scheme JS1 is more uniform compared to the original scheme, resulting in a more stable water flow entering the pump. The color of the velocity cloud for the optimized scheme JS1 changes less, especially in the edge area. This indicates that the velocity distribution of the optimization scheme is more uniform than that of the original scheme, making the water flow entering the pump more stable. This greatly reduces the vortices and cavitation in the water pump, improving its service life.

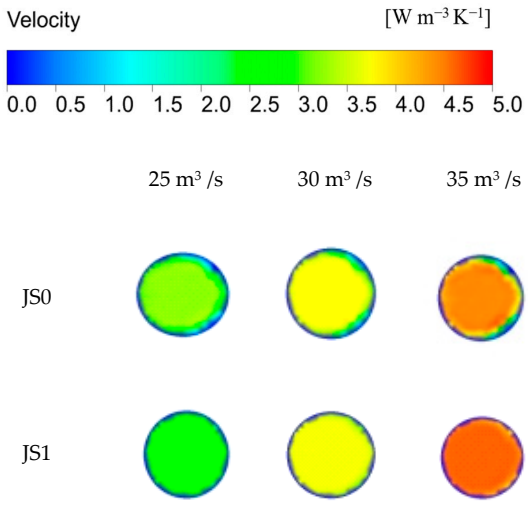


Figure 12. Velocity cloud of the pump inlet section.

Compared with the original design scheme, the hydraulic performance of the inlet channel was enhanced to varying degrees in all operating conditions for the several opti-

mized schemes, especially for JS1 and JS3, which show significant improvements. The JS1 scheme performs best in terms of hydraulic loss, the velocity-weighted average angle, and axial-velocity distribution uniformity and was therefore selected as the optimal scheme. This scheme demonstrates lower hydraulic losses than the initial scheme across all flow conditions, proving the effectiveness of the optimization design.

4. Further Optimization of Inlet Channel

Although the optimal scheme has shown considerable improvement in hydraulic performance over the initial scheme, there remains a disparity in comparison to the anticipated outcomes, necessitating further refinement. To determine the distribution of hydraulic losses, it is essential to calculate the entropy production associated with these losses.

4.1. The Application of the Entropy Production Theory in the Optimization of the Inlet Channel

The entropy generation theory can quantify flow losses in the form of entropy generation. By calculating the distribution of the entropy generation rate in the internal flow field of hydraulic machinery, it is possible to determine the specific values and locations of losses; explore, in-depth, the causes of flow losses; and thus optimize the design scheme.

Although the entropy generation theory can effectively reveal the mechanisms and distributions of energy losses, it may face certain limitations when simulating these complex flow phenomena. For instance, in flow separation regions, the entropy generation theory may not be able to accurately capture the position of the separation point and the detailed structure of the separation vortex, which affects the precise assessment of hydraulic losses. Additionally, in the turbulent transition region, the calculation accuracy of the entropy generation theory may also be influenced to some extent. This is because the turbulent transition process involves the interaction of vortices at multiple scales, and the entropy generation theory may have certain deficiencies in handling multi-scale flows.

There are also challenges that the entropy generation theory may encounter in practical engineering applications. Firstly, in actual projects, the geometric shape of the inlet channel of a pumping station can be extremely complex, with various irregular boundary conditions, such as local protrusions, depressions, and non-uniform wall roughness. These complex geometric and boundary conditions pose challenges to the calculation accuracy and stability of the entropy generation theory, potentially leading to certain deviations in the calculation results. Secondly, the application of the entropy generation theory requires a large amount of computational resources and time, especially in large-scale three-dimensional numerical simulations. The high computational cost may limit its application in some engineering projects with limited resources. Moreover, the parameter settings and model calibration of the entropy generation theory require high-level professional knowledge and experience, which may pose some difficulties for non-professionals to apply it.

Therefore, we needed to analyze the feasibility of the entropy generation theory in this research project.

4.1.1. Feasibility Analysis of Calculating Losses Using Entropy Production Theory

Based on the entropy production theory, the total direct dissipation (EPDD) and turbulent dissipation (EPTD) in each part of the computational domain can be obtained through volume integration in the post-processing of numerical simulations, and wall dissipation (EPWS) can be obtained through the integration of the wall's surface area. The sum of these three components represents the total energy dissipation in the region. The traditional method for calculating hydraulic losses relies on measuring the pressure difference between the inlet and outlet of hydraulic machinery. Therefore, to assess the precision of the entropy production theory in calculating energy losses, nine different flow

conditions for the initial scheme of the inlet channel were calculated. The hydraulic losses obtained using the entropy production method were compared with those calculated using the pressure difference method, as shown in Figure 13 and Table 6.

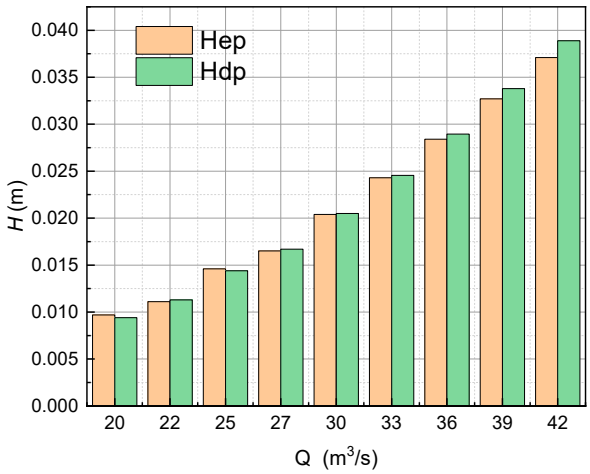


Figure 13. Hydraulic losses under different operating conditions using the entropy production method and the pressure difference method.

Table 6. Comparison of entropy production method and pressure difference method for hydraulic losses.

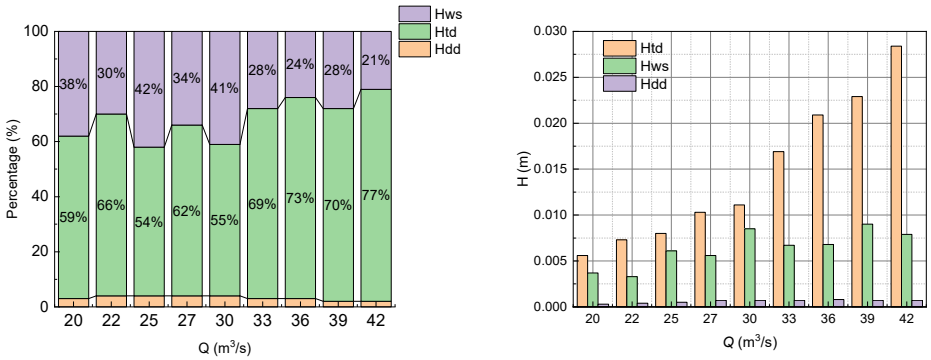
Q (m^3/s)	H_{ep}(m)	H_{dp}(m)	Relative Error (%)
20	0.0097	0.0094	3.01%
22	0.0111	0.0113	2.04%
25	0.0146	0.0144	1.44%
27	0.0165	0.0167	0.97%
30	0.0204	0.0205	0.59%
33	0.0243	0.02455	1.08%
36	0.0284	0.02895	1.82%
39	0.0327	0.0338	3.37%
42	0.0371	0.0389	4.70%

According to Figure 13, the trends of hydraulic losses calculated by both methods vary similarly with the flow rate, and the results are in close agreement, especially near the rated operating condition, where the hydraulic losses are minimized. As the operating condition deviates from the optimal one, the deviation between the results obtained by the two methods gradually increases. Nevertheless, Table 3 indicates that the relative errors between the hydraulic losses calculated using the entropy production method (H_{ep}) and those calculated using the pressure difference method (H_{dp}) are all less than 5%, falling within an acceptable range. This confirms the reasonableness and credibility of the entropy production method for calculating hydraulic losses. Therefore, the entropy production method can accurately predict the hydraulic losses in the inlet and outlet channel. Furthermore, compared to the pressure difference method, the entropy production method provides a more direct approach to studying the energy dissipation characteristics of the inlet and outlet channel.

4.1.2. Comparative Analysis of Head Losses Caused by Various Entropy Production Components

To more intuitively illustrate the factors contributing to the changes in hydraulic losses in the inlet channel with the flow rate, a comparison of various entropy production terms

was conducted. The hydraulic losses calculated using the entropy production method consist of direct dissipation, turbulent dissipation, and wall dissipation. Through integration, the hydraulic losses caused by each of them were calculated separately. Specifically, the hydraulic loss due to direct dissipation is h_{dd}, the hydraulic loss due to turbulent dissipation is h_{td}, and the hydraulic loss due to wall dissipation is h_{ws}. The results are shown in Figure 14.



(**a**) (**b**)

Figure 14. Proportion of hydraulic losses caused by various entropy generation components. (**a**) Proportion of hydraulic losses caused by each entropy production item. (**b**) Hydraulic losses caused by each entropy production item.

Figure 14a illustrates the proportion of hydraulic losses contributed by three entropy production terms. Across all flow conditions, the hydraulic losses in the inlet channel are primarily attributed to turbulent dissipation and wall dissipation, which together constitute more than 95% of the total hydraulic loss. Therefore, turbulent dissipation and wall dissipation are the primary contributors to the energy losses observed in the inlet channel.

Figure 14b depicts the variation in different hydraulic losses with flow rates. It can be observed from this figure that the hydraulic loss caused by turbulent dissipation follows the same trend as the inlet channel loss shown in Figure 13, gradually augmenting with the flow rate. However, the hydraulic loss due to wall dissipation does not exhibit a clear trend with an increasing flow rate and does not align with the overall trend of the total hydraulic loss. Regarding the hydraulic loss caused by direct dissipation, it remains almost constant regardless of flow rate changes. Therefore, the variation in energy loss in the inlet channel is primarily driven by turbulent dissipation. Turbulence dissipation is associated with turbulent kinetic energy, and drastic changes in turbulent kinetic energy can lead to rapid growth in turbulent dissipation. When vortex or flow separation occurs in fluid flow, it can alter the turbulent kinetic energy. Possibly, under off-design conditions, vortex or flow separation in the flow field of an inlet channel may result in increased hydraulic losses.

4.1.3. Analysis of Hydraulic Loss in Inlet Flow Channels Based on Entropy Production Theory

From the preceding analysis, it is evident that the variation in energy loss in the inlet channel across various flow conditions is primarily driven by turbulent dissipation. Therefore, the key to further optimizing the design lies in analyzing the distribution contours of turbulent dissipation so as to cut down the energy loss. The results calculated for the initial model and the JS1 scheme of the inlet channel at the rated flow rate were imported into the CFD-POST 2023 software to obtain the distribution of turbulent dissipation, as shown in Figure 15.

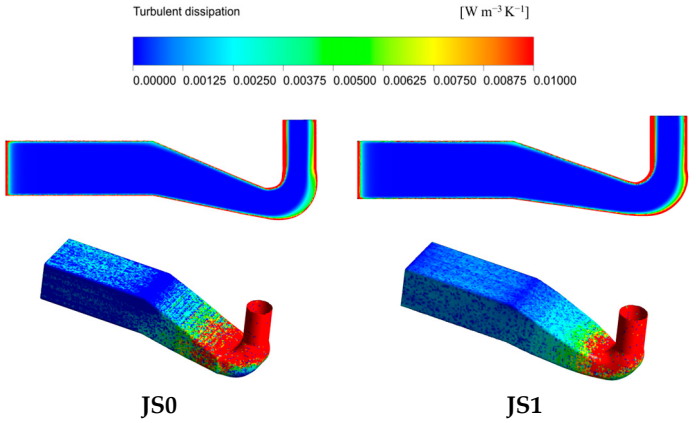


Figure 15. Distribution of turbulent dissipation.

Figure 15 shows that the overall entropy production distribution is similar between the optimized scheme and the initial scheme. The red areas indicate the highest wall dissipation, primarily concentrated around the elbow bends, highlighting the critical importance of optimizing the elbow section.

Additionally, the elevation of an inlet channel directly impacts project costs, and channel optimization must balance hydraulic performance with economic benefits. Therefore, considering practical engineering constraints, further in-depth optimization of the JS1 scheme will focus on the elevation of the inlet channel and the cross-sectional width (throat width, B_h). Table 7 shows the parameters of each scheme, while Figure 16 presents their front and top views.

Table 7. Specific parameters of the scheme for further optimizing the influent flow channel.

	X_w (mm)	X_r (mm)	β (°)	B_h (mm)	Q (m^3/s)
JS1-1	3650.8/1981.8	10,682.9	8	6100	30
JS1-2	3650.8/1981.8	10,682.9	8	7500	30
JS1-3	3455.7/2361.4	10,682.9	10	4850	30
JS1-4	3455.7/2361.4	10,682.9	10	7500	30

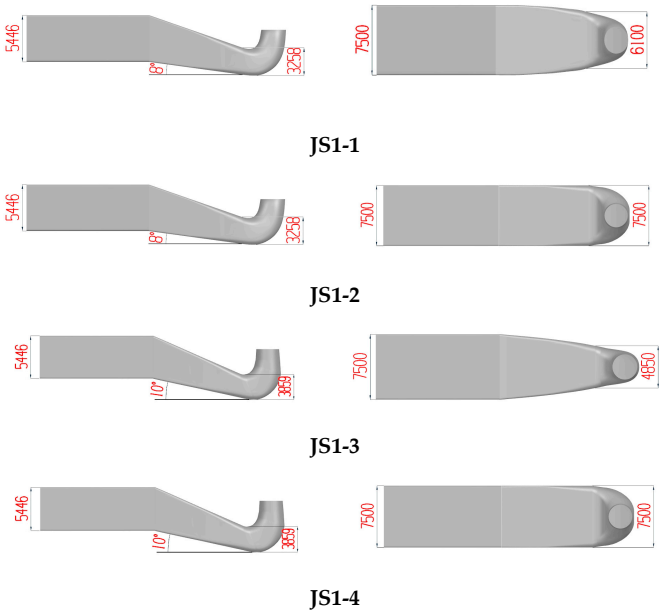


Figure 16. Model diagrams of inlet channels for various design schemes.

4.2. Calculation of Inlet Channel for Further Optimization of External Characteristics

From Figure 17, it can be seen that the optimized scheme JS1-3 has the minimum amount of hydraulic loss, and the velocity-weighted average angle is the largest, approaching 90°. JS1-2 and JS1-3 have the most uniform axial-velocity distribution, nearing 100%.

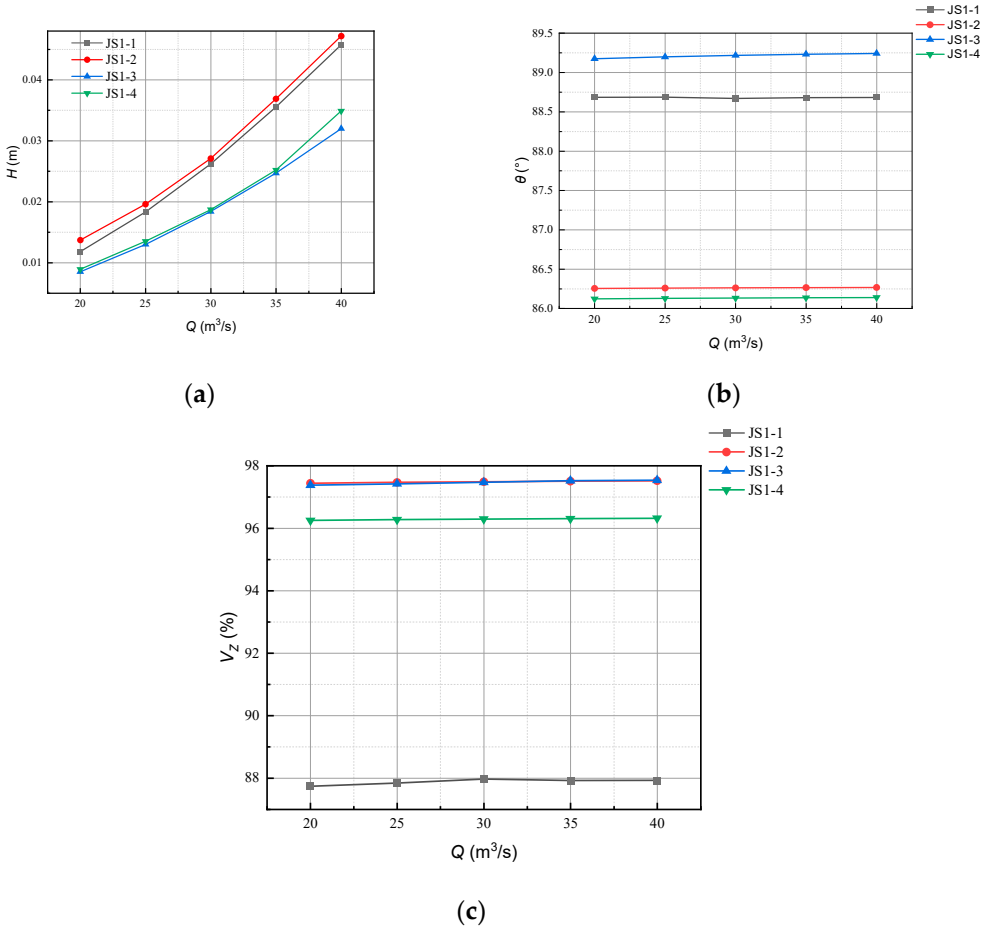


Figure 17. Hydraulic performance evaluation curve. (**a**) Hydraulic loss–flow curve. (**b**) Velocity-weighted average angle–flow curve. (**c**) Velocity distribution uniformity–flow curve.

4.3. Flow Field Analysis of Inlet Channel for Further Optimization

The boundary shape and roughness of an inlet channel are important factors in the formation of vortices. When water flows through the bends, the cross-section changes, or areas with protrusions exist in the inlet channel, due to the sudden change in boundary conditions, the velocity and pressure distribution of the water flow change, causing the streamline to bend, and thus vortices are formed. The presence of vortices significantly increases the head loss in the inlet flow channel and disrupts the originally relatively uniform velocity distribution within the inlet flow channel. As shown in Figure 18, the vorticity distribution in JS1-3 is less at the wall surface and in the curved parts. After comprehensively evaluating the hydraulic losses of various schemes and thoroughly analyzing their internal flow field characteristics, it can be concluded that Scheme JS1-3 is the optimal choice.

To further analyze the flow patterns within the pump system before and after optimization, five sections (V1, V2, V3, V4, and V5) were selected along the channel cross-section.

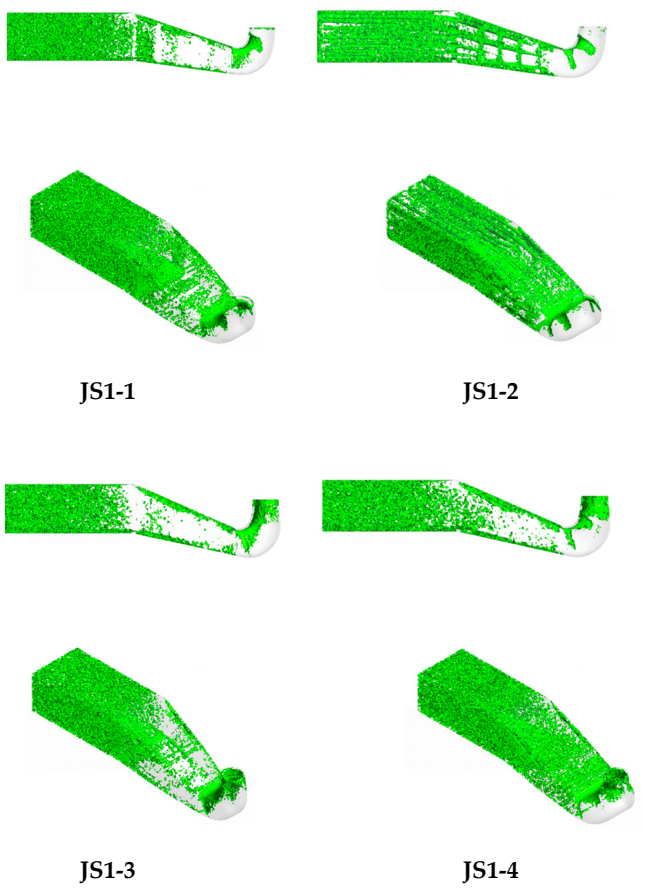


Figure 18. Vorticity diagram.

As seen in Figures 19 and 20, the velocity distribution follows a pattern where the flow velocity is higher on the inner side of the passage and lower on the outer side, with a left–right symmetrical distribution. Before entering the elbow section (V1 and V2 sections), the flow is relatively smooth, and the velocity distribution is more even. After entering the elbow section (V3–V5 sections), the velocity on the inner side increases significantly, and the flow pattern becomes more turbulent. The optimized channel cross-section is smoother and more uniform compared to the pre-optimization state, resulting in better flow patterns, particularly evident in the V2 and V4 sections.

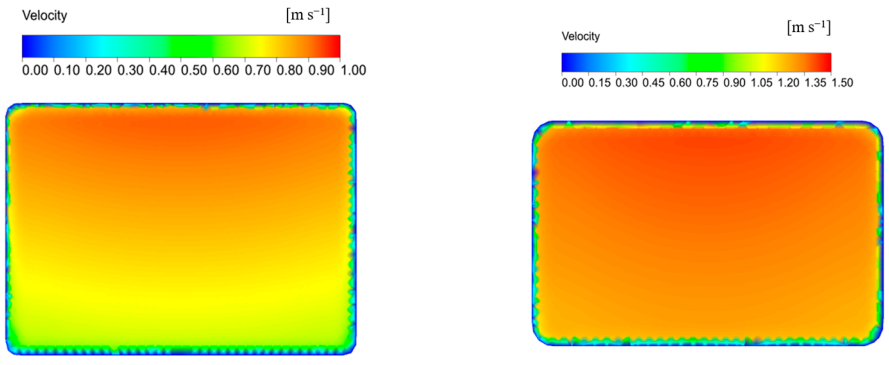


Figure 19. *Cont.*

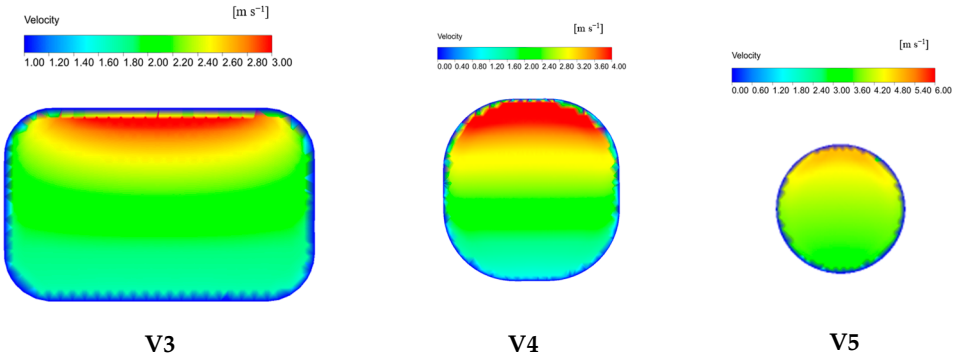


Figure 19. Velocity cloud of the inlet channel cross-section before optimization.

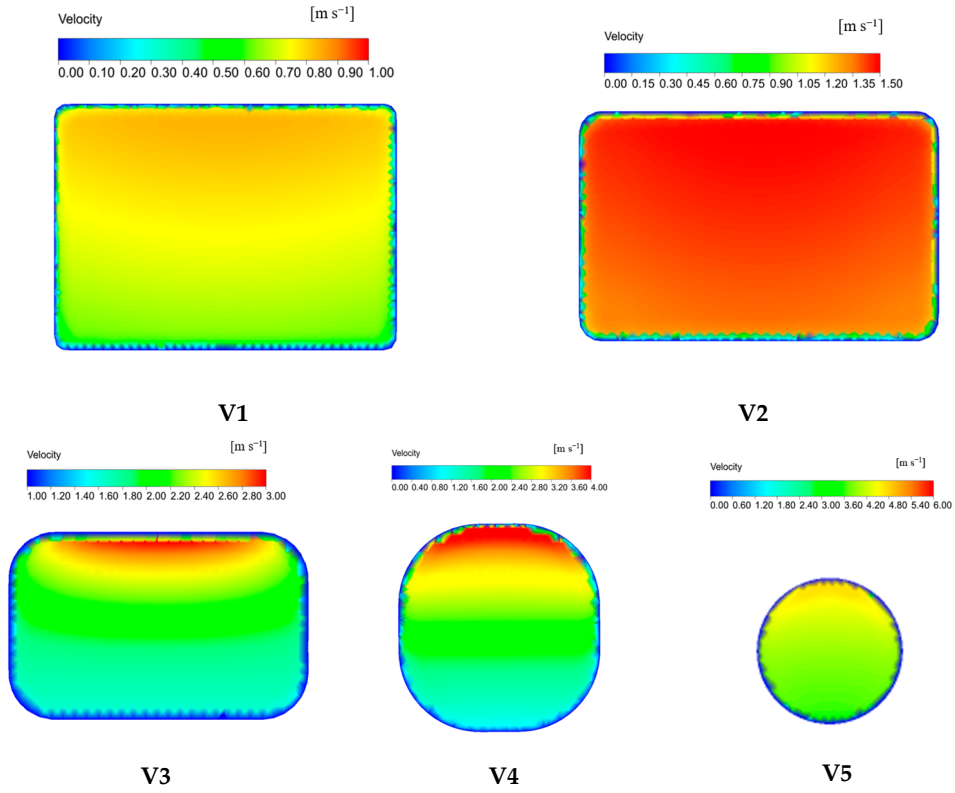


Figure 20. Velocity cloud of the inlet channel cross-section after optimization.

5. Economic and Feasibility Analysis

From the perspective of construction costs, the optimized plan adjusts the geometric shape of the inlet channel of the pumping station. These adjustments may increase the construction difficulty and workload to some extent, thus leading to an increase in construction costs. However, in the long run, the optimized design can significantly improve the operation efficiency and reliability of the pumping station and reduce energy consumption and maintenance costs, thereby bringing greater economic benefits during the operation phase and offsetting part of the increase in construction costs. In addition, the optimized design can extend the service life of the pumping station and reduce the additional costs caused by equipment damage and replacement.

Regarding technical feasibility, current construction technologies and equipment capabilities are sufficient to meet the implementation requirements of the optimized design plan. Modern surveying technologies and construction equipment can accurately measure and construct complex geometric shapes, guaranteeing the precise realization of every parameter in the optimized plan. Moreover, the materials and construction techniques

adopted in the optimized design are all well-established and reliable, posing no significant technical risks to the construction process.

During the secondary optimization of JS1, we attempted to reduce the earthwork excavation volume and the quantity of canal lining work by lowering the elevation of the inlet flow channel, thereby reducing construction costs. However, calculations showed that this increased the flow velocity and head loss, resulting in a decline in hydraulic performance. Reducing the cross-sectional width, on the other hand, could reduce the occupied area of the canal and the consumption of building materials, further saving costs. Unlike reducing the elevation, this approach did not cause a significant decline in hydraulic performance. Instead, after adjusting the smoothness of the cross-section, the hydraulic performance further improved. Ultimately, we chose the JS1-3 scheme, which maintains the bottom elevation of the inlet flow channel and reduces the cross-sectional width. The long-term benefits of the JS1-3 scheme, such as energy conservation, consumption reduction, and increased operational efficiency, keep the investment payback period within an acceptable range, making it highly cost-effective.

6. Conclusions

In this paper, considering the characteristics of the pumping station and aligning with the project's research objectives, an optimization design of a pumping station's inlet channel was conducted through numerical calculations. First, preliminary optimization was conducted, and an optimized model was obtained. Subsequently, more detailed optimization was further carried out based on this model. The key conclusions obtained are as follows:

(1) The SBES model is capable of better describing the properties of various flow parameters with a shorter computational time. The trend of the wall friction coefficient curve obtained by the SBES model aligns more closely with experimental values, greatly facilitating the treatment of the boundary layer. Applying the SBES model to the design and optimization of an elbow inlet channel can serve as a valuable reference for similar engineering projects.

(2) The difference between the hydraulic losses calculated using the entropy production method and the pressure difference method is minimal. The entropy production theory can reveal the energy loss mechanism in the channel, clarify the primary origins and distribution of energy loss, and provide clear goals and directions for channel optimization.

(3) Each optimized scheme outperforms the initial scheme to some extent in terms of overall hydraulic losses, the outlet velocity-weighted average angle, axial-velocity distribution uniformity, streamline distributions, and velocity and pressure distributions in the longitudinal section. Among them, the JS1 scheme is the best. This proves the effectiveness of the optimization and suggests that controlling the inclination angle of the base plate within 8–10° and appropriately increasing the length of the transition arc section within a reasonable range can improve the hydraulic performance of the inlet channel.

(4) The elevation and section width of the inlet channel have an impact on its hydraulic performance, and generally, a design with a smaller section width tends to exhibit better hydraulic performance. On the basis of JS1, the inlet runner elevation and section width were optimized in depth, and the weighted average exit velocity angle of the JS1-3 scheme reaches 89.25°, the uniformity of axial-velocity distribution reaches 97.5%, and the hydraulic performance is excellent.

(5) During the planning and construction phases of the pumping station, various factors, including hydraulic performance, economic costs, and construction feasibility, should

be comprehensively considered. In order to achieve the overall optimality of a design plan, systematic, optimized design methods, such as multi-level decision-making analyses and weighted scoring, should be adopted.

The research of this paper is based on the SBES model. It is recommended that future research explore the application of other advanced turbulence models in the optimization of a pumping station inlet channel, such as the large-eddy simulation (LES) model, the Detached-Eddy Simulation (DES) model, etc. This would further improve the accuracy and reliability of numerical simulations and would more precisely capture complex turbulent phenomena and flow details. In addition, it is proposed to integrate emerging technologies such as artificial intelligence and machine learning to conduct research on the intelligent optimization design and operational control of the pumping station inlet channel. This aims to achieve intelligent and refined management of the pumping station, thereby enhancing its operational efficiency and economic benefits.

Author Contributions: Software, X.Y.; Validation, Y.Z. (Yi Zhang); Investigation, J.Z., B.C. and Y.Z. (Yi Zhang); Resources, Y.T.; Writing—original draft, R.J.; Writing—review & editing, Y.Z. (Yuan Zheng) and H.D. All authors have read and agreed to the published version of the manuscript.

Funding: The authors would like to acknowledge the financial support given by the National Natural Science Foundation of China (No. 52209109).

Data Availability Statement: Data are contained within the article.

Conflicts of Interest: The authors declare no conflict of interest.

References

1. Jones, G.M.; Bosserman, B.E.; Sanks, R.L.; Tchobanoglous, G. *Pumping Station Design*, 3rd ed.; Elsevier: Amsterdam, The Netherlands; Butterworth-Heinemann: Oxford, UK, 2008.
2. Gan, X.C.; Pavesi, G.; Pei, J.; Yuan, S.Q.; Wang, W.J.; Yin, T.Y. Parametric investigation and energy efficiency optimization of the curved inlet pipe with induced vane of an inline pump. *Energy* **2022**, *240*, 122824. [CrossRef]
3. Hu, C.H.; Wu, W.; Hu, J.B.; Yuan, S.H. Flow dynamical behavior and performance of a micro viscous pump with unequal inlet and outlet areas. *Eng. Appl. Comput. Fluid Mech.* **2016**, *10*, 443–453. [CrossRef]
4. Choi, J.W.; Choi, Y.D.; Kim, C.G.; Lee, Y.H. Flow uniformity in a multi-intake pump sump model. *J. Mech. Sci. Technol.* **2010**, *24*, 1389–1400. [CrossRef]
5. Rajendran, V.P.; Patel, V.C. Measurement of vortices in model pump-intake bay by PIV. *J. Hydraul. Eng.* **2000**, *126*, 322–334. [CrossRef]
6. Dimas, A.A.; Vouros, A.P. Effect of Cross-Flow Velocity at Forebay on Swirl in Pump Suction Pipe: Hydraulic Model of Seawater Intake at Aliveri Power Plant in Greece. *J. Hydraul. Eng.* **2012**, *138*, 812–816. [CrossRef]
7. Mittag, S.; Gabi, M. Experimental and Numerical Investigation of Centrifugal Pumps with Asymmetric Inflow Conditions. *J. Therm. Sci.* **2015**, *24*, 516–525. [CrossRef]
8. Lin, F.; Wang, X.; Guan, Z.W.; Hu, J.Y.; Wang, Z.N.; Liang, Q.W. Model experimental study on special frequency of hydraulic pump working condition headcover for ultra-high head pump-turbine. *J. Phys. Conf. Ser.* **2024**, *2752*, 012076. [CrossRef]
9. Kim, J.H.; Lee, H.C.; Kim, J.H.; Choi, Y.S.; Yoon, J.Y.; Yoo, I.S.; Choi, W.C. Improvement of Hydrodynamic Performance of a Multiphase Pump Using Design of Experiment Techniques. *J. Fluids Eng.* **2015**, *137*, 081301. [CrossRef]
10. Jin, J.M.; Ji, H.G.; Kim, Y.J. Optimal Design for Impeller of a Sludge Pump Using Design of Experiment. In Proceedings of the ASME-JSME-KSME 2019 8th Joint Fluids Engineering Conference, San Francisco, CA, USA, 28 July–1 August 2019. [CrossRef]
11. Sexton, C.J.; Lewis, S.M.; Please, C.P. Experiments for derived factors with application to hydraulic gear pumps. *J. R. Stat. Soc. Ser. C (Appl. Stat.)* **2001**, *50*, 155–170. [CrossRef]
12. Zhao, P.; Bai, Y.C. Study on Hydraulic Characteristics and Optimization of Siphon Channel with Two Inlets in Drydock. *Appl. Mech. Mater.* **2014**, *638*, 1285–1292. [CrossRef]
13. Jiang, H.J.; Yuan, Z.L.; Chang, M.W. Error Analysis of Trial Data on the Pump Trial Stage. *IOP Conf. Ser. Earth Environ. Sci.* **2017**, *94*, 012048. [CrossRef]
14. Yan, H.Y.Y.; Heng, Y.G.; Zheng, Y.; Tao, R.; Ye, C.L. Investigation on Pressure Fluctuation of the Impellers of a Double-Entry Two-Stage Double Suction Centrifugal Pump. *Water* **2022**, *14*, 4065. [CrossRef]

15. Sun, X.; Xu, H.Z.; Xuan, X.X.; Manickam, S.; Boczkaj, G.; Wang, B.L. Assessing the industrialization progress of hydrodynamic cavitation process intensification technology: A review. *Curr. Opin. Chem. Eng.* **2024**, *45*, 101037. [CrossRef]
16. Kan, K.; Chen, H.X.; Zheng, Y.; Zhou, D.Q.; Binama, M.; Dai, J. Transient characteristics during power-off process in a shaft extension tubular pump by using a suitable numerical model. *Renew. Energy* **2021**, *164*, 109–121. [CrossRef]
17. Xia, G.J.; You, W.B.; Manickam, S.; Yoon, J.Y.; Xuan, X.X.; Ab, X.S. Numerical simulation of cavitation-vortex interaction mechanism in an advanced rotational hydrodynamic cavitation reactor. *Ultrason. Sonochem.* **2024**, *105*, 106849. [CrossRef]
18. Yang, W.B.; Peng, S.J.; Xiao, W.H.; Hu, Y.F.; Wu, H.C.; Li, M. CFD-Based Flow Channel Optimization and Performance Prediction for a Conical Axial Maglev Blood Pump. *Sensors* **2022**, *22*, 1642. [CrossRef]
19. Shrestha, U.; Choi, Y.D. Estimation of Reverse Flow Rate in J-Groove Channel of AJP and SCP Models Using CFD Analysis. *Processes* **2022**, *10*, 785. [CrossRef]
20. Sujono, H.; Haribowo, R.; Purwanto, T.S. Attempts to reduce cavitation phenomena at the Ciawi Dam inlet conduit using CFD Modeling. *IOP Conf. Ser. Earth Environ. Sci.* **2024**, *1311*, 012010. [CrossRef]
21. Cheng, B.; Yu, Y.H. CFD Simulation and Optimization for Lateral Diversion and Intake Pumping Stations. *Procedia Eng.* **2012**, *28*, 122–127. [CrossRef]
22. Xie, C.L.; Xuan, W.P.; Feng, A.N.; Sun, F. Analysis of Hydraulic Performance and Flow Characteristics of Inlet and Outlet Channels of Integrated Pump Gate. *Water* **2022**, *14*, 2747. [CrossRef]
23. Sha, L.; Yang, S.; Kong, X.; Sun, H.; Pei, L. Influence of inlet flow field uniformity on the performance of the nuclear main pump. *IOP Conf. Ser. Mater. Sci. Eng.* **2021**, *1081*, 012024. [CrossRef]
24. Turabi, H.; Zheng, Y.; Maxime, B. Effect of stationary diffuser size on performance and pressure field characteristics of an axial-flow pump in pump mode. *J. Braz. Soc. Mech. Sci. Eng.* **2023**, *45*, 170. [CrossRef]
25. Yu, Y.; Yan, H.; Ye, C. Parameter optimization of rectification sill in the forebay of pumping station using BPNN-GA algorithm. *Trans. Chin. Soc. Agric. Eng.* **2023**, *39*, 106–113.
26. Li, C.X.; Zhao, G.Y.; Zhao, Y.G.; Fu, W.Z.; Zheng, Z.F. Research on hydraulic loss of liquid ring vacuum pump and optimization of shell profile for high efficiency and energy saving. *Vacuum* **2023**, *207*, 111633. [CrossRef]
27. Ji, L.L.; Li, W.; Shi, W.D.; Chang, H.; Yang, Z.Y. Energy characteristics of mixed-flow pump under different tip clearances based on entropy production analysis. *Energy* **2020**, *199*, 117447. [CrossRef]
28. Zhou, L.; Hang, J.W.; Bai, L.; Krzemianowski, Z.; El-Emam, M.A.; Yasser, E.; Agarwal, R. Application of entropy production theory for energy losses and other investigation in pumps and turbines: A review. *Appl. Energy* **2022**, *318*, 119211. [CrossRef]
29. Eves, J.; Toropov, V.V.; Thompson, H.M.; Kapur, N.; Fan, J.; Copley, D.; Mincher, A. Design optimization of supersonic jet pumps using high fidelity flow analysis. *Struct. Multidiscip. Optim.* **2012**, *45*, 739–745. [CrossRef]
30. Adhav, R.S.; Samad, A.; Kenyery, F. Optimal designs of an ESP to handle upto 10% GVF. *Int. J. Oil Gas Coal Technol.* **2016**, *13*, 338–358. [CrossRef]
31. Safikhani, H.; Khalkhali, A.; Farajpoor, M. Pareto Based Multi-Objective Optimization of Centrifugal Pumps Using Cfd, Neural Networks and Genetic Algorithms. *Eng. Appl. Comp. Fluid Mech.* **2011**, *5*, 37–48. [CrossRef]
32. Kim, M.S.; Seong, H.S.; Yang, J.H.; Lee, S.W.; Choi, S.W. Fluid Flow and Effect of Turbulence Model on Large-Sized Triple-Offset Butterfly Valve. *J. Appl. Fluid Mech.* **2023**, *16*, 2364–2380. [CrossRef]
33. In, W.K.; Chun, T.H. Assessment of the rans turbulence models for a turbulent flow and heat transfer in a rod bundle. *Nucl. Technol.* **2005**, *150*, 231–250. [CrossRef]
34. Tian, M. Optimized design of inflow conduits based on numerical simulation. *Water Wastewater Eng.* **2015**, *41*, 103–106.
35. Hao, Y.; Tan, L. Symmetrical and unsymmetrical tip clearances on cavitation performance and radial force of a mixed flow pump as turbine at pump mode. *Renew. Energy* **2018**, *127*, 368–376. [CrossRef]
36. Gul, M.Z.; Yangaz, M.U.; Sen, S. A Two-Time-Scale Turbulence Model and Its Application in Free Shear Flows. *Appl. Sci.* **2024**, *14*, 1133. [CrossRef]
37. Sun, Y.; Zhu, W.; Wu, Y.; Qi, H. The applicability study of Gao-Yong turbulence model to boundary layer transitions. *J. Tsinghua Univ. Sci. Technol.* **2023**, *63*, 642–648.
38. Kan, K.; Yang, Z.X.; Lyu, P.; Zheng, Y.; Shen, L. Numerical study of turbulent flow past a rotating axial-flow pump based on a level-set immersed boundary method. *Renew. Energy* **2021**, *168*, 960–971. [CrossRef]
39. Ye, C.L.; An, D.S.; Huang, W.R.; Heng, Y.G.; Zheng, Y. Investigation on Stall Characteristics of Centrifugal Pump with Guide Vanes. *Water* **2023**, *15*, 21. [CrossRef]
40. Menter, F.; Hüppe, A.; Matyushenko, A.; Kolmogorov, D. An Overview of Hybrid RANS-LES Models Developed for Industrial CFD. *Appl. Sci.* **2021**, *11*, 2459. [CrossRef]
41. Zore, K.; Aliaga, C.N.; Selva, J.; Zori, L.A.J.; Makarov, B. High-Fidelity SBES Simulations for Supersonic Nozzle Exhaust Flows. In Proceedings of the AIAA SciTech 2024 Forum, Orlando, FL, USA, 8–12 January 2024.
42. Kim, B.C.; Chang, K. Assessment of Hybrid RANS/LES Models in Heat and Fluid Flows around Staggered Pin-Fin Arrays. *Energies* **2020**, *13*, 3752. [CrossRef]

43. Ye, C.; Wang, C.; Yan, H.; Wang, F.; Zheng, Y.; van Esch, B. Investigation on transition characteristics of laminar separation bubble on a hydrofoil. *Phys. Fluids* **2023**, *35*, 105154. [CrossRef]
44. Zhao, H.R.; Wang, F.J.; Wang, C.Y.; Ye, C.L.; Yao, Z.F.; Zhong, Q. A modified VLES model for simulation of rotating separation flow in axial flow rotating machinery. *J. Hydrodyn.* **2022**, *34*, 570–584. [CrossRef]
45. Wang, C.; Wang, F.; Ye, C.; Wang, B.; Zou, Z. Application of the MST turbulence model to predict the tip leakage vortex flows. *Eng. Comput.* **2021**, *38*, 344–353. [CrossRef]
46. Ye, C.L.; Wang, C.Y.; Zi, D.; Tang, Y.; van Esch, B.P.; Wang, F.J. Improvement of the SST γ-R$e_{\theta t}$ transition model for flows along a curved hydrofoil. *J. Hydrodyn.* **2021**, *33*, 520–533. [CrossRef]
47. Sun, Z.Z.; Yu, J.; Tang, F.P. The Influence of Bulb Position on Hydraulic Performance of Submersible Tubular Pump Device. *J. Mar. Sci. Eng.* **2021**, *9*, 831. [CrossRef]
48. Zhang, L.B.; Luo, Y.; Shen, Z.H.; Ye, D.X.; Li, Z.H. Optimization Design of the Elbow Inlet Channel of a Pipeline Pump Based on the SCSO-BP Neural Network. *Water* **2024**, *16*, 74. [CrossRef]

Disclaimer/Publisher's Note: The statements, opinions and data contained in all publications are solely those of the individual author(s) and contributor(s) and not of MDPI and/or the editor(s). MDPI and/or the editor(s) disclaim responsibility for any injury to people or property resulting from any ideas, methods, instructions or products referred to in the content.